Journal of Solid State Chemistry **148,** 3–15 (1999)
Article ID jssc.1999.8190, available online at http://www.idealibrary.com on IDEAL®

High-Temperature Electrical Property and Defect Analysis of the Quintuple Perovskite Layered Cuprates $Eu_2CaBa_2Cu_2Ti_3O_{14}$ and $LaYCaBa_2Cu_{2+x}Ti_{3-x}O_{14-y}$

M. H. Kane,* N. Mansourian-Hadavi,* T. O. Mason,*,[1] W. Sinkler,* L. D. Marks,* K. D. Otzschi,†,[2] D. Ko,† and K. R. Poeppelmeier†

*Materials Science and Engineering Department, Northwestern University, 2225 N. Campus Drive, Evanston, Illinois 60208-3108; and †Department of Chemistry, Northwestern University, Evanston, Illinois 60208

Received July 30, 1998; in revised form February 1, 1999; accepted February 5, 1999

High-temperature electrical conductivity and thermopower measurements have been performed on undoped $Eu_2CaBa_2Cu_2Ti_3O_{14}$ and doped and undoped $LaYCaBa_2Cu_{2+x}Ti_{3-x}O_{14}$. These quintuple perovskites are members of a family of ordered perovskite-type oxides with double Cu–O sheets and have in-plane Cu–O bond lengths comparable to known superconductors. X-ray diffraction data and transmission electron microscopy show clear evidence of layering in both structures. $LaYCaBa_2Cu_{2+x}Ti_{3-x}O_{14}$ exhibits a large-small rare earth ordering on the A'/A'' sites, like its quadruple perovskite counterparts. The transport data indicate that these materials behave similarly to the corresponding quadruple perovskites, but have lower carrier concentrations. The La–Y compound exhibits weaker oxygen partial pressure dependencies in the electrical properties, which are suggestive of a decrease in undesirable oxygen intercalation between the CuO_2 sheets. Upon doping with copper on titanium sites, (Cu''_{Ti}), a concomitant amount of oxygen vacancies, ($V_o^{\bullet\bullet}$), are introduced, as evidenced by TGA and *in situ* electrical property measurements. Possible defect models are presented and discussed in light of data from TGA, electrical property measurements, and quantitative high-resolution TEM. © 1999 Academic Press

Key Words: **electrical conductivity; thermopower; point defects; cuprates; electron microscopy.**

INTRODUCTION

Since the discovery of high T_c superconductors (1), a number of common structural features have been observed which are now deemed essential for supporting high temperature superconductivity, e.g., 2-D layering, with copper–oxygen sheets separated by blocks of insulating material, the latter serving as a charge reservoir and bond-mismatch layer for the Cu–O sheets. These "conditioning layer" blocks may be of a number of different structures, including rocksalt, as in $La_{2-x}AE_xCuO_4$ and the BSSCO compounds, and fluorite, as in $Nd_{2-x}Ce_xCuO_4$. Alternatively, the conditioning layer can consist of oxygen-deficient perovskite layers, as in $YBa_2Cu_3O_7$ (i.e., the chain sites) and in $YSr_{1-x}Ca_xGaCu_2O_7$, which has oxygen-stoichiometric gallate tetrahedra in the conditioning layer.

No known high T_c superconductors have pure titanate perovskite blocks in the conditioning layer. This is thought to be due to the long in-plane Cu–O bond lengths in these compounds. Typical in-plane bond lengths in the known *p*-type superconductors range from 1.90 to 1.95 Å. In the known quadruple perovskites, the smallest in-plane Cu–O bond length is 1.947 Å in $NdDyBa_2Ti_2Cu_2O_{11}$ and $Tb_2Ba_2Cu_2Ti_2O_{11}$ (2,3), though it can be considerably longer as in the case of $RE_2Ba_2Cu_2Ti_2O_{11}$ materials, where RE = La, Eu, La, or Nd (4–6). These long bond lengths are a result of the long Ti–O bond lengths in the titanate conditioning layer. Since one of the functions of the conditioning layer is to impart either compression or tension to the Cu–O sheets in order to promote hole or electron formation (7), respectively, it is important for there to be a bond-mismatch between the conditioning and active layers. Holes are stabilized in "compressive" materials, where the conditioning layer bond lengths are smaller than in the active layer (7). In the quadruple perovskites, the average Ti–O (or Sn–O) bond lengths are close to the natural Cu–O bond length for copper in square pyramidal coordination. As such, there is no real driving force for the production of holes, and these materials have insufficient carrier concentrations for superconductivity. Upon aliovalent doping, these compounds exhibit ionic compensation (oxygen vacancies) as opposed to the desired electronic

[1]To whom correspondence should be addressed. E-mail: t-mason@nwu.edu.

[2]Present address: Department of Applied Chemistry, University of Tokyo, Tokyo, Japan.

0022-4596/99 $30.00

compensation (2, 8–10). Refilling of these structural vacancies has been largely unsuccessful, though in the smallest bond length quadruple perovskites, some limited reoxidation of the Cu–O planes has been observed via slow cooling, high oxygen pressure treatments, or electrochemical methods (2, 9–11).

The present work reports an attempt to engineer the architecture of quintuple pure-perovskite layered cuprates, in particular by reducing the in-plane Cu–O bond length, with the goal of developing new superconducting materials. Quintuple, e.g., $Sm_2CaBa_2Cu_2Ti_3O_{14}$ (12), and sextuple, e.g., $Dy_2Ca_2Ba_2Cu_2Ti_4O_{17}$ (13), pure perovskite layered cuprates have been recently obtained through addition to the quadruple perovskite structures of $CaTiO_3$ perovskite layers. Subsequently, a number of other members of these families have been found (14, 15).

In situ high-temperature four-point electrical conductivity and thermopower measurements have proven useful tools for establishing hole-doping efficacy in layered cuprates and to screen for potential high T_c superconductivity (16–18). In particular, Jonker Plots (19) (thermopower vs logarithm of conductivity) and Brouwer plots (20) (thermopower vs logarithm of doping level or of oxygen activity) can be used to assess carrier contents, prevailing defect regimes, and transport parameters.

This report details high-temperature electrical property measurements of the undoped quintuple perovskites, $Eu_2CaBa_2Cu_2Ti_3O_{14}$ and $LaYCaBa_2Cu_2Ti_3O_{14}$. In addition, transport property measurements on doped $LaYCaBa_2Cu_{2+x}Ti_{3-x}O_{14}$ at compositions of $x = 0.2$ and 0.4 are reported and correlated with oxygen stoichiometry data obtained via thermogravimetry (TGA). Based upon these data and high-resolution transmission electron microscopy observations, possible vacancy models for the location of oxygen defects are considered, along with ramifications for high T_c superconductivity.

EXPERIMENTAL PROCEDURE

Samples were prepared by solid-state reaction of stoichiometric mixtures of Ln_2O_3 (Ln = Eu, La, Y), $AECO_3$ (AE = Ba, Ca), CuO, and TiO_2, all of phase purity above 99.99%. Before mixing, the La_2O_3 was heated at 600°C for 1 h to convert any hydroxide back into the oxide, and the carbonates were annealed in CO_2 to ensure stoichiometry. The reagents were ground and fired at 950°C in high-density alumina boats in air for 1 day and air quenched, after which they were pelletized. The pellets were then fired at 1050°C over the course of a 3–7 day reaction period, with several intermediate regrindings. Sacrificial pellets of the same composition were employed to prevent reaction with the alumina boats utilized.

Phase analysis was performed by X-ray diffraction using a Scintag XDS 2000 diffractometer (Scintag Inc., Cupertino, CA) with filtered Cu$K\alpha$ radiation on quenched polycrystalline samples. Data were collected with a 2θ scan from 15° to 90° with a step size of 0.02° and a sample collection time of 10 s at each step. Silicon was used as an internal standard. The structure was fit to a tetragonal $a_p \times a_p \times 5a_p$ unit cell to determine the lattice parameters.

Hydrogen reduction thermogravimetry was performed using a thermogravimetric analyzer (TA Instruments 2950, New Castle, DE). Samples were first equilibrated in flowing oxygen for 8 h at 800°C, then reduced in a 7% H_2/N_2 mixture to known compounds, which were then identified using X-ray diffraction.

High-resolution transmission electron microscopy (HRTEM) was performed using an Hitachi H9000 microscope operated at 300 kV. Data were collected on photographic negatives and scanned using a microdensitometer (Optronics P1000, Chelmsford, MA). For quantitative comparison with simulated images, the data were scaled to unit unscattered beam intensity. Image simulation was performed using NUMIS software developed at Northwestern University, and all image processing used SEMPER VI software (Synoptics, Cambridge, UK).

Simultaneous 4-pt dc conductivity and thermopower measurements were performed using an apparatus described elsewhere (21). From the pressed and sintered pellets of quintuple perovskites, rectangular parallelepiped bars were cut and notched using a low speed diamond saw. Gold foil was used as the outer electrodes, whereas the inner electrodes were tight loops of 10-mil gold wire. Pt/90Pt–10Rh thermocouples were in contact with each electrode to measure the temperature at the four electrode positions. Samples were equilibrated in oxygen or oxygen–argon premixtures at oxygen partial pressures ranging from 10^{-5} to 1 atm. A steady state "straddle" technique, employing the natural thermal gradient of the furnace, was employed for thermopower measurements. A current reversal/averaging procedure was used to eliminate thermal e.m.f.s from conductivity measurements. Data were taken at temperatures of 650°, 700°, 750°, and 800°C. Electrical conductivity was corrected for the porosity of the sample using a Bruggeman asymmetric medium model for the porosity, which is described elsewhere (22).

Jonker analysis (19) was employed in analysis of the electrical property data. The technique, originally used for the analysis of semiconductors, consists of plotting thermopower versus the natural logarithm of conductivity (see Fig. 1). Plots are often called Jonker "pears," given their characteristic shape, and are a function of the intrinsic conductivity, the bandgap, and scattering mechanisms. Transport asymmetry can also be seen in the fitting of these pears. An iterative Matlab (The MathWorks, Natwick, MA) program (23) was used to calculate and fit the acquired data to a symmetric Jonker Pear, by varying both the bandgap (which governs the size of the pear) and the

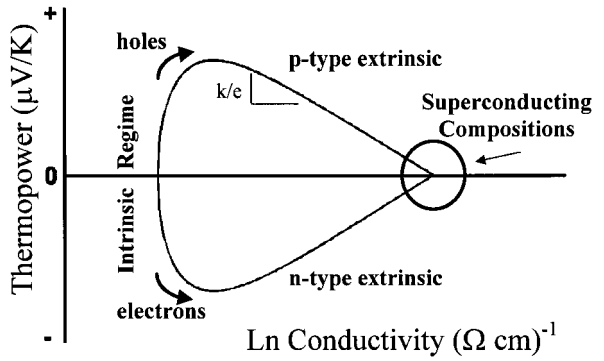

FIG. 1. Schematic of a Jonker pear, showing intrinsic and extrinsic (*p*-type, *n*-type) regimes. For layered cuprates, superconducting compositions occur near the vertex.

intrinsic conductivity (which governs the position along the *x* axis).

Important features to note on these Jonker pears are that the sign of the thermopower gives the sign of the majority carrier. Carrier concentration increases clockwise around the diagram for holes and counterclockwise for electrons. The backside of the pear (low conductivity) represents the intrinsic conduction region, where two-band conduction dominates and the thermopower changes rapidly with small changes in conductivity. The linear regions of the pear are the extrinsic regions, where one carrier type dominates the transport properties. The ideal slope of these legs is $\pm k/e$, where k is Boltzmann's constant and e is electron charge, and the high-conductivity intersection of each leg is determined by the product of density-of-states and mobility. It should be noted that the superconducting compositions are all toward this high-conductivity intercept of the pear, where sufficient carriers have been introduced. For a more detailed description of this technique, the reader is referred to the literature (16, 19).

Brouwer Analysis (20) was also employed to analyze for prevailing defect regimes. In these plots the defect concentration (or an electrical property related to the defect concentration) is plotted as a function of dopant level or oxygen partial pressure. This technique enables various defect models to be tested against the slopes of these curves within each defect regime.

RESULTS AND DISCUSSION

$Eu_2CaBa_2Cu_2Ti_3O_{14}$

Phase-pure samples of $Eu_2CaBa_2Cu_2Ti_3O_{14}$ were successfully produced by solid state reaction. X-ray diffraction confirmed the presence of a single, quintuple perovskite layered cuprate, the structure of which is shown in Fig. 2. The average structure exhibits *P*4/*mmm* space group symmetry with lattice parameters $a = 3.8828(7)$ Å and $c = 19.576(7)$ Å. An HRTEM image is also shown in Fig. 3, in which the layered structure of copper–oxygen planes, separated by three perovskite blocks, is easily observed. Right-angle domains were observed in some of the micrographs, but relatively few stacking defects were present.

The oxygen content determined by hydrogen-reduction thermogravimetry was 14.03 ± 0.05, consistent with 1/15 of the perovskite oxygen positions being vacant. These vacancies occur between the Cu–O planes, resulting in the square pyramidal oxygen coordination, as shown in Fig. 2. The $Eu_2CaBa_2Cu_2Ti_3O_{14}$ structure has been recently published (15). Ba^{2+} resides at the large A^* site adjacent to the copper pyramids. Europium occupies the A'' between the adjacent copper oxygen sheets, whereas the other A' site is occupied by the Eu^{3+} and Ca^{2+} cations. It should be noted that this is analogous to the previously reported quadruple perovskite $Eu_2Ba_2Cu_2Ti_2O_{11}$ (24).

The electrical property behavior of quintuple $Eu_2CaBa_2Cu_2Ti_3O_{14}$ is shown in the Jonker plots of Fig. 4. The samples exhibited positive thermopower values, as expected for a *p*-type semiconductor. The thermopower values tended to lie along the back (intrinsic) to extrinsic portions of the pear, indicating that these samples are lightly hole-doped, though at lower values than for the related quadruple perovskite. This is not unusual for the parent compounds in superconducting systems; a number of

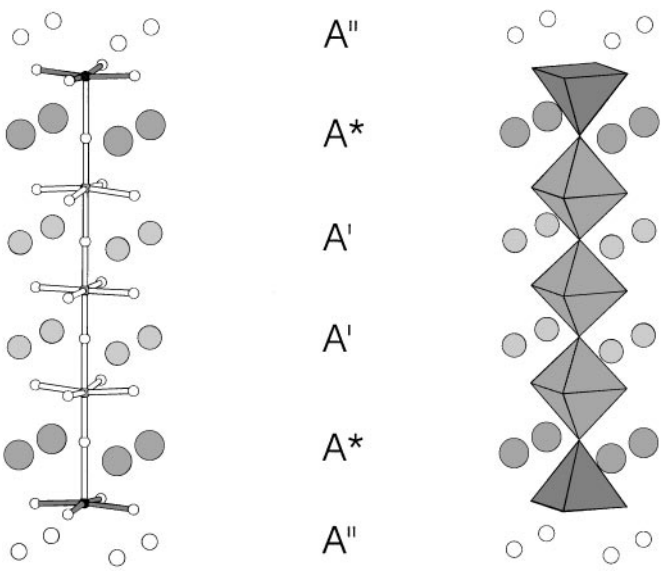

FIG. 2. Ball-and-stick and polyhedral representations of the quintuple perovskite structures. The titanate octahedra are in middle of the structure, with copper-oxygen square pyramids at either end. The CuO_2 sheets are shown by the bonds labeled in black. The remaining spheres in the structure represent the alkaline earth and rare earth atoms in the structure. The A^* site is the largest site and is occupied by Ba^{2+}. The A'' is the smallest site and is occupied by Eu^{3+} or Y^{3+}. The A' site is occupied by the remaining rare earth and alkaline earth cations.

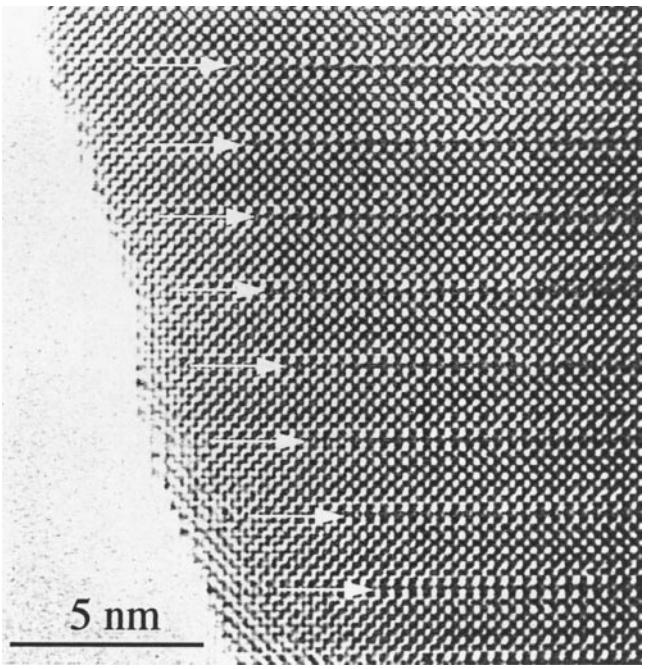

FIG. 3. HRTEM image of $LaYCaBa_2Cu_2Ti_3O_{14}$ along the [100] direction. The five-layered structure is clearly visible. The active layer (base-facing CuO_5 pyramids) are shown in the faint lines running horizontally through the sample, indicated by the arrows. Between these areas, the three titanate layers and are clearly visible.

superconductors have been found to exhibit similar behavior in the undoped state. The exact origin of the extrinsic behavior (slight preference for hole doping) is not known, but is likely due to small deviations from cation and/or anion stoichiometry. As a general rule, "compressive" cuprates tend to exhibit this slightly doped *p*-type behavior, even in their parent compounds (2, 6, 16, 17, 23). The hole contents are quite small, however, as evidenced by the large values of thermopower.

Additional insight can be obtained from the high-conductivity intercept and a comparison with the corresponding quadruple perovskite behavior in Fig. 4. There appears to be no detectable variation of intercept with temperature for a given composition, which is consistent with the behavior of other layered cuprates (2, 6, 16, 17, 25), indicating that the density-of-states (DOS)-mobility product is independent of temperature. In comparison, the quadruple perovskite has a significantly larger DOS-mobility product, more so than can be accounted for on the basis of the increased density of copper ions in this structure. Furthermore, as noted previously, the quadruple perovskite has a slightly higher carrier content as shown in the more pronounced extrinsic behavior. Nevertheless, the undoped parent compounds behave somewhat similarly.

The transport parameters obtained from the Jonker plot fits are given in Table 1, and for comparison, the Jonker fit parameters for the undoped quadruple perovskite $Eu_2Ba_2Cu_2Ti_2O_{11}$ are also shown. As can be seen, the bandgaps obtained from the Jonker fits are very similar between the two materials. This would suggest that the electronic structure is not significantly altered by the presence of an additional titanate block. Since the electronic transport in these compounds is believed to be dominated by the copper–oxygen sheets, this is not unexpected.

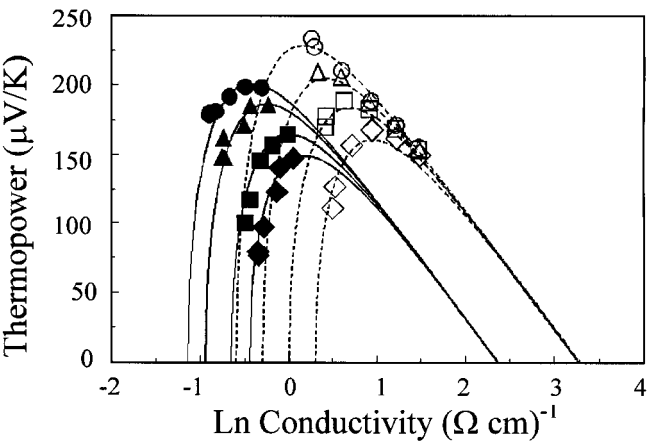

FIG. 4. Jonker pears fitted to the measured $Eu_2CaBa_2Cu_2Ti_3O_{14}$ data (solid symbols). For comparison, the values reported in (10) for the related quadruple perovskite $Eu_2Ba_2Cu_2Ti_2O_{11}$ are also displayed (open symbols). Symbols are as follows: circles, 650°C; triangles, 700°C; squares, 750°C; and diamonds, 800°C. Oxygen partial pressure increases clockwise around each pear from 10^{-5} to 10^{-4}, 10^{-3}, 10^{-2}, 10^{-1}, and 1 atm.

$LaYCaBa_2Cu_{2+x}Ti_{3-x}o_{14}$ ($x = 0, 0.2, 0.4$)

The quintuple perovskite, $LaYCaBa_2Cu_{2+x}Ti_{3-x}O_{14}$ system, is analgous to the previously reported $LaYBa_2Cu_2Ti_2O_{11}$ quadruple perovskite (2). Both the quintuple

TABLE 1
Jonker Fitting Parameters for $Eu_2CaBa_2Cu_2Ti_3O_{14}$ (Fig. 4) and $Eu_2Ba_2Cu_2Ti_2O_{11}$ (6), Assuming Band Conduction to be Operative (16)

Temp.	$\ln \sigma_i$	$\ln \sigma_{max}$	Eg (eV)
	$Eu_2CaBa_2Cu_2Ti_3O_{14}$		
923 K	− 1.15	2.37	0.352
973 K	− 0.95	2.37	0.339
1023 K	− 0.66	2.37	0.306
1073 K	− 0.45	2.37	0.282
	$Eu_2Ba_2Cu_2Ti_2O_{11}$		
923 K	− 0.60	3.3	0.41
973 K	− 0.30	3.3	0.38
1023 K	0.00	3.3	0.35
1073 K	0.30	3.3	0.31

and quadruple perovskite systems can be doped with copper on the titanium sites. The $LaYCaBa_2Cu_{2+x}Ti_{3-x}O_{14}$ system is particularly advantageous relative to the europium quintuple perovskites for two reasons. First, we have been able to introduce copper into the system over the range $x = 0.0$ to 0.4 (possibly as high as $x = 0.6$), as indicated by XRD and TEM. Traces of impurity phases are present in the doped samples, as evidenced by single unidentified impurity peaks, whose positions corresponds to $Ln_2Cu_2O_5$ or $CaTiO_3$. Both a birefringent transparent phase and a transparent nonbirefringent impurity phase were visible in transmission optical microscopy of crushed powders of compounds in this system. Lattice parameters changed continuously, however, across this composition range (*a* axis: 3.8843(4), 3.8881(6), and 3.8939(7) for $x = 0$, 0.2, and 0.4, respectively; *c* axis: 19.616(4), 19.633(2), and 19.651(9) for $x = 0$, 0.2, and 0.4, respectively). At $x = 0.6$ and above, the $LaYCaBa_2Cu_{2+x}Ti_{3-x}O_{14}$ samples showed more significant impurity peaks and quadruple perovskite superlattice peaks (26). Second, this compound exhibits a large–small A'/A''-type arrangement, giving two distinct lanthanide sites. Since the yttrium cation is much smaller than the lanthanum cation (e.g., compare 1.019 vs 1.16 Å in eightfold coordination, as per Ref. (27)), these two atoms can be expected to order based on the preference of smaller cations for lower coordinate sites. In the quadruple perovskite, yttrium was observed to lie in the site between the copper oxygen sheets, whereas the larger lanthanum cation was observed to lie in the larger A' sites between the titanate blocks (10). This was evidenced in the electrical property measurements by decreased partial pressure dependencies of both conductivity and reduced thermopower in the quadruple perovskite measurements. The smaller lanthanide, yttrium, makes the intercalation of oxygen between the copper–oxygen sheets energetically unfavorable, hence the reduced partial pressure dependence of the electrical properties. A similar behavior is observed in the La–Y cuprate and will be analyzed further below. Since the inclusion of oxygen interstitials between the Cu–O sheets is thought to be detrimental to superconductivity, the introduction of the smaller yttrium cation is thought to be beneficial with respect to achieving superconductivity in these materials.

Thermogravimetric analysis of the $LaYCaBa_2Cu_{2+x}Ti_{3-x}O_y$ materials at the compositions $x = 0.0$, 0.2, and 0.4 gave oxygen contents of the system to be 14.01 ± 0.05, 13.79 ± 0.05, and 13.57 ± 0.05, respectively. These values are consistent with nominally divalent copper. Rather than the intended electronic compensation mechanism ($h^{\bullet} = 2[Cu''_{Ti}]$), an ionic compensation mechanism predominates (i.e., $[V^{\bullet\bullet}_O] = [Cu''_{Ti}]$. This is consistent with the previous reports for *B*-site cation substitutions in quadruple perovskites (2, 8, 9). Specific defect models are discussed below.

The results of the combined high temperature electrical property measurements are shown in Fig. 5a. These are compared with the results from the $LaYBa_2Cu_2O_{11}$ quadruple perovskite. As in the europium family, the quintuple perovskite shows a decrease in both the magnitude of the conductivity and the number of carriers, as indicated by the position on the Jonker pear. All of the values lie along the extrinsic leg of the pear, indicating a higher number of carriers in the La–Y compounds versus the Eu–Eu family. Although the high-conductivity intercept can be reliably obtained on the basis of Fig. 5a, there is considerable uncertainty in the band gap values, owing to so little influence of minority electrons; the data are removed from the top of their Jonker plots. Therefore, these band-gap values are

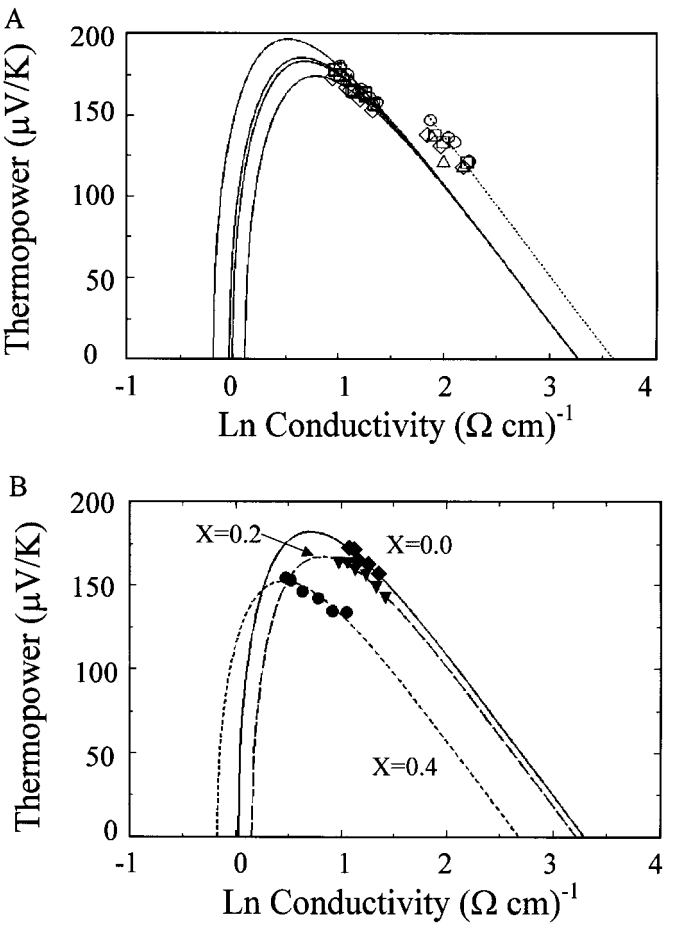

FIG. 5. (a) Jonker pears fitted to the measured $LaYCaBa_2Cu_2Ti_3O_{14}$ data (on the left). For comparison, the values reported in [2] for the related quadruple perovskite $LaYBa_2Cu_2Ti_2O_{11}$ are also displayed (to the right). Symbols are as follows: circles, 650°C; triangles, 700°C; squares, 750°C; and diamonds, 800°C. Oxygen partial pressure increases clockwise around each pear from 10^{-5} to 10^{-4}, 10^{-3}, 10^{-2}, 10^{-1}, and 1 atm. (b) Jonker plots at 750°C for quintuple perovskite $LaYCaBa_2Cu_{2+x}Ti_{3-x}O_{14-y}$ vs doping level ($x = 0.0$, 0.2, 0.4). Oxygen partial pressure increases clockwise around each pear from 10^{-5} to 10^{-4}, 10^{-3}, 10^{-2}, 10^{-1}, and 1 atm.

enclosed with parentheses in Table 2. Note also the absence a typical variation in band gap with temperature as compared to the undoped Eu-based materials in Table 1, most likely a consequence of the uncertainty in fitting.

Upon doping (Fig. 5b), there is little change in the thermopower of $LaYCaBa_2Cu_{2+x}Ti_{3-x}O_{14}$, which indicates that the desired doping mechanism is not taking place, in agreement with the TGA results. There are minor changes in the conductivity values as x increases from 0 to 0.4. The position of points on the Jonker Pear also shifts back toward the intrinsic region as observed by the noticeable decrease in slope. This is consistent with the decrease observed in band gap upon doping (see Table 2). As the bandgap decreases, more electron–hole pairs are created by thermal excitations. Since the relative ratio of holes-to-electrons is decreased, the points will move back toward the intrinsic region of the pear.

The LaY quintuple perovskites exhibit very small, almost negligible slopes on their Brouwer plots (log conductivity vs log pO_2) in Fig. 6. This has been previously explained for the quadruple perovskites (4) as an elimination of oxygen intercalation between the Cu–O sheets. The slope of this line increases very slightly with the introduction of copper into the conditioning layer at $x = 0.2$ and 0.4.

Defect Model in the Intrinsic Regime

It is apparent from Fig. 6 that the oxygen partial pressure dependence for the undoped europium quintuple perovskite is larger than it is for the undoped lanthanum yttrium quintuple perovskite. This is consistent with the quadruple perovskite behavior (2), where large–large rare-earth perovskites exhibited $+1/6$ slopes in their log σ vs log pO_2 plots, but the large–small rare-earth perovskites exhibited shallow, virtually zero slopes on similar plots. This $+1/6$ slope is consistent with oxygen interstitial formation by the defect reaction

$$\tfrac{1}{2}O_2(g) \rightarrow O_i'' + 2h^{\bullet};\ K_O p_{O_2}^{1/2} = [O_i'']p^2 \qquad [1]$$

under the electroneutrality conditon of

$$p = 2\,[O_i'']. \qquad [2]$$

The oxygen interstials were believed to be located in the empty oxygen site between the copper–oxygen planes in large/large rare-earth perovskite $Eu_2Ba_2Cu_2Ti_2O_{11}$. Recent evidence for the incorporation of oxygen between the copper–oxygen planes was reported for the large/large *RE* quintuple perovskite, $Nd_2Ba_2CaCu_2Ti_3O_{14}$, based upon Rietveld analysis of powder neutron diffraction data (28). Through the introduction of the small Y^{3+} ion sheets, oxygen is thought to be excluded from these sites, as evidenced by the lack of an oxygen partial pressure dependence in the electrical properties.

It should be noted that the slope in Fig. 6 is significantly less than the anticipated $+1/6$ for the La–Y quintuple perovskite. This arises due to the influence of minority electrons on the overall conductivity. By introducing the parameter a

$$a = \frac{p}{n_i} = \frac{n_i}{n}, \qquad [3]$$

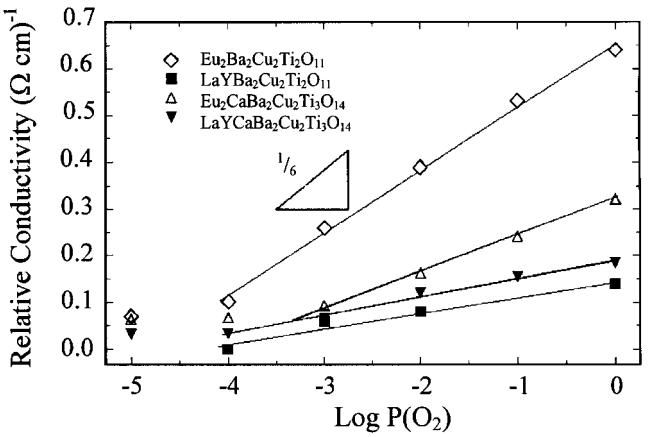

FIG. 6. Brouwer plot of log (conductivity) vs log (oxygen partial pressure) for Eu–Eu (open symbols) vs La–Y (solid symbols) perovskites. Data are shifted from their measured 700°C values; measured log σ data at 1 atm are (in S/cm): $Eu_2Ba_2Cu_2Ti_2O_{11} = 0.640$; $Eu_2CaBa_2Cu_2Ti_3O_{14} = -0.203$; $LaYBa_2Cu_2Ti_2O_{11} = 0.966$; $LaYCaBa_2Cu_2Ti_3O_{14} = 0.583$. The quadruple perovskite data are taken from (6).

TABLE 2

Jonker Fitting Parameters for $LaYCaBa_2Cu_2Ti_3O_{14}$ (Fig. 5a), $LaYBa_2Cu_2Ti_2O_{11}$ (Fig. 5a), and $LaYCaBa_2Cu_{2+x}Ti_{3-x}O_{14-y}$ (Fig. 5b) Assuming Band Conduction to be Operative (16)

Temp.	$\ln \sigma_i$	$\ln \sigma_{max}$	Eg (eV)
	$LaYCaBa_2Cu_2Ti_3O_{14}$		
923 K	− 0.19	3.27	(0.344)
973 K	− 0.02	3.27	(0.334)
1023 K	− 0.04	3.27	(0.354)
1073 K	0.11	3.27	(0.344)
	$LaYBa_2Cu_2Ti_2O_{11}$		
923 K	—	3.6	—
	$LaYCaBa_2Cu_{2+x}Ti_{3-x}O_{14-y}$		
1023 K ($x = 0$)	− 0.04	3.27	(0.354)
1023 K ($x = 0.2$)	0.15	3.22	(0.311)
1073 K ($x = 0.4$)	− 0.18	2.68	(0.275)

Note. Band gap values are uncertain due to the location of the data on the relevant Jonker plots (see text).

where p is the hole concentration, n is electron concentration, and n_i is the intrinsic carrier concentration, it can be shown that

$$\frac{d\ln\sigma}{d\ln P_{O_2}} = \frac{(a^2-1)^2}{2(a^2+1)(3a^2+1)}. \quad [4]$$

The derivation is given in the Appendix and is based on the defect reaction, Eq. [1], and

$$\text{null} \rightarrow e' + h^{\bullet};\ K_i = np \quad [5]$$

combined with a simplified electroneutrality condition:

$$p = n + 2[O_i'']. \quad [6]$$

The value of a is related to the ratio of conductivity (σ) to the intrinsic conductivity (see Appendix):

$$a = \frac{\sigma}{\sigma_i} + \sqrt{\frac{\sigma^2}{\sigma_i^2} - 1}. \quad [7]$$

Figure 7a shows a plot of log conductivity vs $\log pO_2$ slope against the ratio of σ/σ_i (measured vs. intrinsic conductivity) according to this model. The inset diagram shows the corresponding points on the Jonker plot. A check of the limits for Eq. [4] shows that as $a \rightarrow 1$, the slope $\rightarrow 0$, as expected for purely intrinsic behavior (point A in the inset of Fig. 7a), and as $a \rightarrow \infty$, the slope $\rightarrow +1/6$ as expected for the purely extrinsic regime (point 'C' in the inset diagram). Intermediate behavior (e.g., point B) corresponds to transitional behavior insofar as pO_2 slope is concerned.

Figure 7b compares measured and model values of pO_2 slope for quadruple and quintuple perovskite Eu–Eu and La–Y layered cuprates. Both Eu–Eu cuprates exhibit behavior close to the model, with the quadruple perovskite showing nearly extrinsic (point C in Fig. 7a) behavior, whereas the quintuple perovskite is clearly transitional (point B in Fig. 7a) in behavior. This suggests, however, that the interstitial oxygen model (Eq. [1]) is valid for both systems. In contrast, the La–Y quadruple and quintuple perovskites exhibit measured slopes which are much less the expected $+1/6$. This suggests that oxygen interstitials are not a major contributing factor to the electrical properties of the large–small rare-earth perovskites.

Another type of Brouwer Plot graphs reduced thermopower ($-Q/2.303(k/e)$) vs the logarithm of aliovalent doping level. Reduced thermopower is proportional to log(carrier concentration), so that this plot can give an indication of how carrier content changes with doping level. As seen in Fig. 8, there is a negligible change in reduced thermopower with doping level in the La–Y quintuple perovskite. This corroborates the prevalent ionic point defect

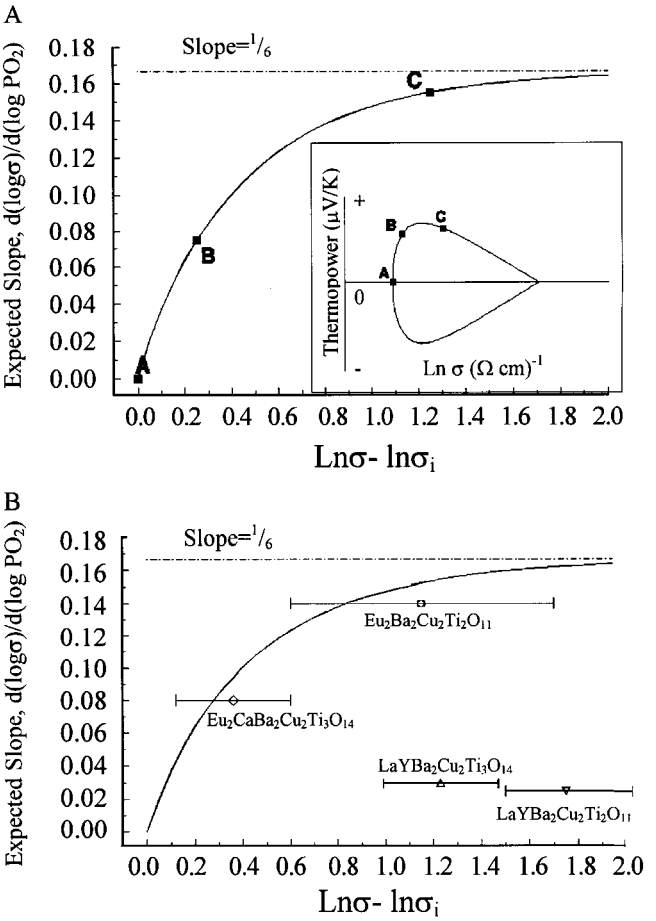

FIG. 7. (a) Anticipated oxygen-Brouwer slopes (as in Fig. 6) based upon the model in the text and Appendix. The inset diagram indicates approximate positions of data on the corresponding Jonker plot. (b) Experimental oxygen-Brouwer slopes (from Fig. 6) compared with the model described in the text and Appendix. The positions of the points indicate the maximum slopes for the material in question. The error bars show the range of $\ln\sigma - \ln\sigma_i$ values for these materials. ($LaYBa_2Cu_2Ti_2O_{11}$ values are approximate, as the sample data exists solely in the extrinsic region so that the complete Jonker pear is uncertain.) The quadruple data are from (6).

mechanism, i.e., $[Cu_{Ti}] = [V_o^{\bullet\bullet}]$. If electronic compensation were occurring, i.e., $p = 2[Cu_{Ti}'']$, there would be a slope of unity on the Brouwer plot.

Vacancy Arrangement Models

Whereas copper can exist in many different coordination environments, titanium prefers strictly octahedral coordination. Taking this into account, it seems likely that the oxygen vacancies introduced by copper substitution will be arranged preferentially so as not to disrupt the octahedral coordination environment of titanium. There are a limited number of possible oxygen vacancy configurations. The combined techniques of electrical property measurements,

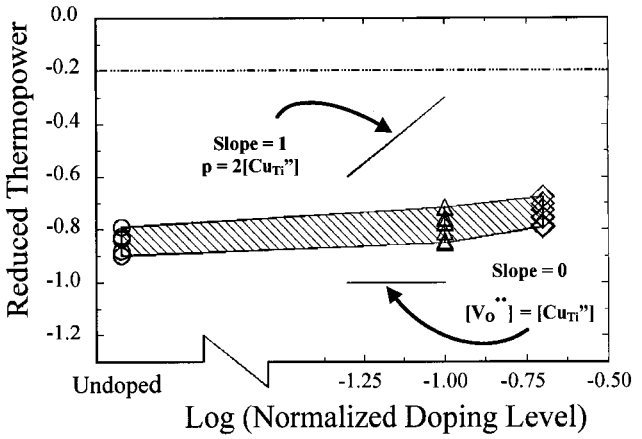

FIG. 8. Brouwer plot (reduced thermopower vs log (doping level)) in the $LaYCaBa_2Cu_{2+x}Ti_{3-x}O_{14-y}$ system, showing that the behavior is consistent with ionic compensation rather than electronic compensation. Circles, triangles, and diamonds are for the undoped, $x = 0.2$, and 0.4 compositions, respectively.

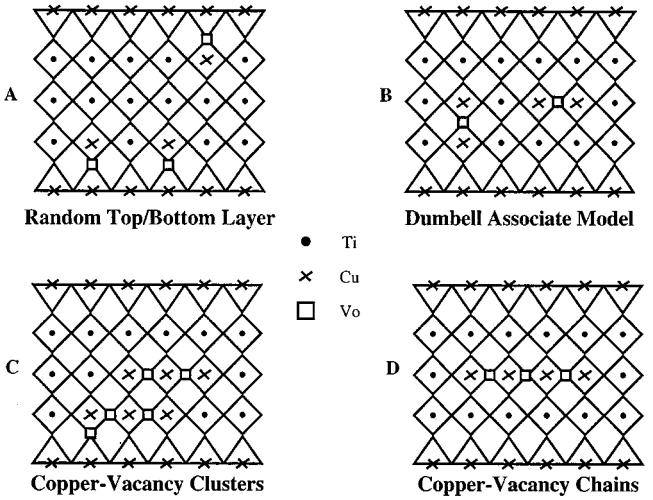

FIG. 9. Models for oxygen vacancy arrangements in the quintuple perovskites. (A) the top/bottom layer vacancy associate model, (B) the dumbell associate model, (C) the copper-vacancy cluster model, and (D) the copper-vacancy chain model.

TGA, and high-resolution TEM (HRTEM) can provide some insight into the relative likelihood of each arrangement.

Figure 9 represents four possible vacancy models which are discussed below. In developing these models, titanium was maintained with strictly octahedral coordination, so that vacancies are allowed to exist only between pairs of copper atoms.

The Random Top/Bottom Titanate Layer Model $(Cu''_{Ti}V^{\bullet\bullet}_{o}Cu^{x}_{Cu})^{x}$

The most likely arrangement (Fig. 9a) introduces a copper atom into the first or third layers of the titanate blocks along with a vacancy between the new copper atom and a copper atom in a conducting plane (i.e., apical oxygen positions with respect to the copper in the Cu–O sheets). In this way, an equal number of copper atoms and oxygen vacancies can be introduced without disrupting the octahedral titanium coordination. Note that this would result in no net increase in the number of carriers, as a neutral associate is formed. The most significant aspect of this model is the preference of copper doping in the top and bottom layers only.

The Dumbbell Associate Model $(Cu'_{Ti}V^{\bullet\bullet}_{o}Cu'_{Ti})^{x}$

Another way to introduce copper atoms and vacancies without disrupting the titanate octahedra places the vacancy in between two copper atoms, yielding two square pyramids in a dumbbell arrangement (Fig. 9b), much like the arrangement of atoms in the Cu–O conducting planes. This is also a neutral associate and should not contribute any carriers, in agreement with the electrical property data. This particular model relies on the presence of trivalent copper in the blocking layer, which is inconsistent with the TGA data. If this were the dominant model, the oxygen content would fall on the middle line in Fig. 10, corresponding to the formula $LaYCaBa_2Cu_{2+x}Ti_{3-x}O_{14-x/2}$. Since this model suggests that one oxygen vacancy would be formed for every two copper atoms, this does not seem to be the prevailing defect arrangement.

Other Models

Two other ways to incorporate copper and oxygen vacancies on a 1:1 (and charge-neutral) basis in the titanate

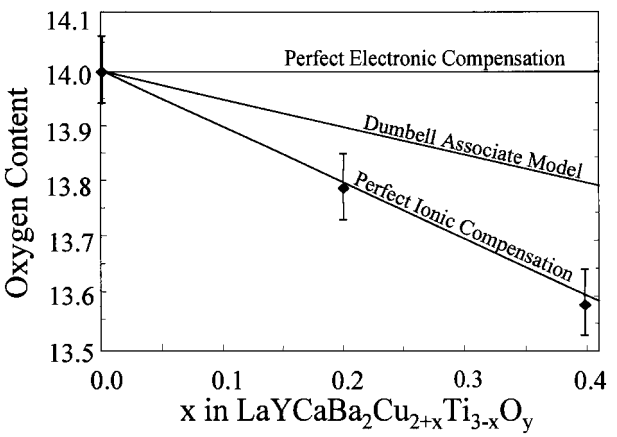

FIG. 10. Oxygen content vs doping in the quintuple perovskite system $LaYCaBa_2Cu_{2+x}Ti_{3-x}O_{14-y}$. The solid lines correspond to electronic compensation ($p = 2[Cu''_{Ti}]$), ionic compensation ($[V^{\bullet\bullet}_{O}] = [Cu''_{Ti}]$, or alternatively the top/bottom copper-vacancy cluster model), and the dumbbell associate model described in the text.

layer without disrupting the octahedral oxygen coordination of titanium is via copper–oxygen vacancy clusters (Fig. 9c) and copper–oxygen vacancy chains (Fig. 9d). (The chain model with n copper and $n-1$ vacancies is not electrically neutral, but requires two holes per chain). Any model characterized by either clustering or ordering in the arrangement of copper and titanium atoms would be expected to result in diffuse scattering or extra reflections in transmission electron diffraction. Since this was not observed as a function of doping, neither model was considered further.

Electron Microscopy

Preliminary TEM observations were used to confirm the layered structure (see Fig. 3) consistent with the XRD results and to characterize the defect structure. In addition to phase identification, high-resolution TEM was combined with image simulation for obtaining structural information concerning cation ordering in order to distinguish among the models presented above. The quantitative use of high-resolution TEM data for obtaining structural information has been applied in the past mainly for obtaining detailed structures of line or planar defects in bulk solids (29–32). In the present study, this relatively new technique was used for obtaining quantitative structure data from a periodic crystal. The overall procedure consists of calculating the image $I_{cal}(\mathbf{r}, p_i)$ based on a number of structural and imaging parameters p_i for points $\mathbf{r}$ in the unit cell. The $I_{cal}(\mathbf{r}, p_i)$ for a through-focus image series are then compared with the experimental images $I_{ex}(\mathbf{r})$ in a through-focus series to obtain the fitness or R factor. By minimizing the R factor, one then arrives at values for the p_i. The minimization of the R factor in the present case involves finding a global minimum in a parameter space with multiple minima. Such problems are well suited for recently developed global search approaches using simulated annealing (33) or genetic algorithms (34). In the present work, a genetic algorithm was used as a search engine for varying the imaging and occupational parameters.

Fitting was performed on two through-focus series. The first series was for the $x = 0$ undoped $LaYCaBa_2Cu_{2+x}Ti_{3-x}O_{14}$ compound and consisted of eight images, and the second for the $x = 0.6$ compound consisted of six images. (The latter composition was selected since it is believed to be close to the solubility limit, thereby maximizing the copper doping.) In bringing the experimental data into a form suitable for comparison with calculated images, a significant simplification was obtained by considering that the quintuple perovskite structure is to a large degree determined by positional and occupational parameters along the c axis. In light of this, fitting of the HREM data to multislice calculations was performed in a one-dimensional scheme, using the image intensity averaged perpendicular to the c axis. This is illustrated in Fig. 11, which shows a [100] experimental image and its projection perpendicular to the c axis for an undoped $LaYCaBa_2Cu_2Ti_3O_{14}$ compound taken at approximately 620 Å underfocus. In the projection, the positions of the heavier A cations and barium correspond to minima, while the positions of the lighter Cu–O and Ti–O layers correspond to maxima. In addition to the use of projections, a further simplification was made in the calculations was the neglect of crystal misorientation. Prior to matching to simulations, the projections were thus symmetry-averaged using a cross-correlation method in order

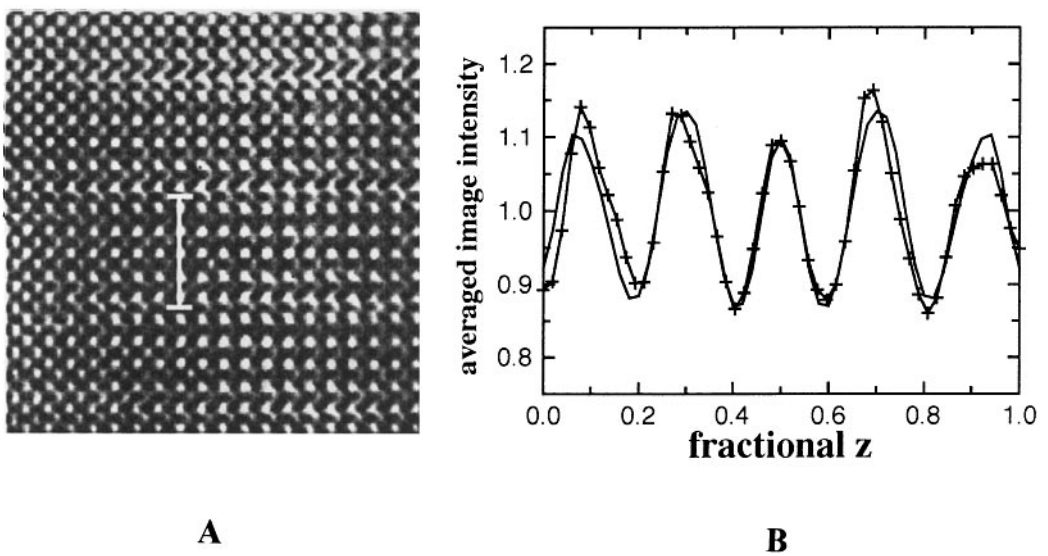

FIG. 11. (a) HRTEM image of $x = 0.6$ doped quintuple perovskite, $LaYCaBa_2Cu_{2+x}Ti_{3-x}O_{14-y}$. (b) Symmetrized ($-$) and unsymmetrized (- + -) intensity projections along the c axis for the HRTEM image shown to the left.

to obtain traces which reproduce the two mirror planes at $z = 0$ and 0.5 in the $P4/mmm$ space group. Figure 11b shows a comparison of the symmetrized and unsymmetrized traces for 620 Å underfocus.

Three different refinements were performed, as summarized in Tables 3 and 4. The solutions given in the Tables are the best obtained in terms of the R factor given by

$$R = \frac{1}{N}\sum_j r_l; \quad r_j = \frac{\sum_i |I_{i,ex} - I_{i,cal}|}{\sum_i I_{i,ex}}, \qquad [8]$$

where the I_i's are the intensities for points i on the experimental and calculated projections, and the r's are the contribution to the total R for the N individual images in the through-focus series. In the calculations, the variation of structural parameters was limited to occupational parameters, which were consistently given 4 bits or 16 possible values. Both the A and B cation order was varied. In the latter case, Cu was allowed to substitute for Ti in the $z = 0.3$ and 0.5 layers. To ionically compensate, oxygen vacancies were introduced into the Ba layer in a concentration equal to the number of Cu atoms on Ti sites. From the outset, it was deemed impossible with this technique to distinguish a mixture of Ca and La from Y. (Yttrium, with atomic number 39, is effectively indistinguishable from a 50% mixture of calcium ($Z = 20$) and lanthanum ($Z = 57$).) The decision was made to abandon this point and concentrate on which atomic column (A' or A'') was heavier or lighter; in varying the A-cation occupational parameters yttrium was treated as an equiatomic mixture of La and Ca. All atomic coordinates were treated as fixed, and the coordinates used were based on XRD Rietveld-refined values for $Eu_2Ba_2CaCu_2Ti_3O_{14}$ from Pack *et al.* (15) In addition to thickness, defocus start, and defocus step, the refinement included variation of the beam convergence angle and a Gaussian smearing in the image plane. The latter tends to slightly reduce the overall contrast level and corresponds to the effect of specimen vibration during recording of the HRTEM image. The value obtained for this parameter was consistent for all refinements, and corresponded to 0.9 Å rms specimen vibration.

TABLE 3
Results from the HREM Structural Refinement of the Undoped Quintuple Perovskite, $LaYCaBa_2Cu_2Ti_3O_{14}$ ($R = 0.0298$)

Parameter	Bits	Range	Resolution	Result
XLa ($z = 0$)	4	0.0–1.0	0.067	0.267
XBa	4	0.0–1.0	0.067	0.933
XCu ($z = 0.3$)	4	0.0–0.6	0.04	0.08
XCu ($z = 0.5$)	4	0.0–0.6	0.04	0.0
Defocus start (Å)	5	− 340–712	12	− 484
Defocus step (Å)	5	− 88–150	2	− 134
Thickness (Å)	5	19.2–138.4	3.8	73
Convergence (mrad)	4	0.7–1.0	0.02	0.98

TABLE 4
Results from the HREM Structural Refinement of the Doped Quintuple Perovskite, $LaYCaBa_2Cu_{2.6}Ti_{2.4}O_y$ ($R = 0.0200$)

Parameter	Bits	Range	Resolution	Result
XLa ($z = 0$)	4	0.0–1.0	0.067	0.200
XBa	4	0.0–1.0	0.067	1.0
XCu ($z = 0.3$)	4	0.0–0.6	0.04	0.24
XCu ($z = 0.5$)	4	0.0–0.6	0.04	0.00
Defocus start (Å)	5	− 64–436	12	− 268
Defocus step (Å)	5	− 88–150	2	− 108
Thickness (Å)	5	57.6–176.6	3.8	77
Convergence (mrad)	4	0.7–1.0	0.02	1.0

Two points concerning the cation ordering emerge from the results of the refinements. First, the refined minimum indicated in each case a significant substitution of calcium for yttrium in the $z = 0$ layer. In terms of the present scheme in which yttrium is represented by an equiatomic mixture of calcium and lanthanum, the best fit in both cases is achieved for La occupancy near $x = 0.2$ (see Tables 3 and 4). The data thus suggest an effective atomic species at the $z = 0$ layer, which is significantly lighter than pure yttrium and corresponds roughly to an equiatomic mixture of yttrium and calcium, using the assumption of no lanthanum substition in the $z = 0$ layer. In order to compensate for this, a somewhat heavier A cation is located at the $z = 0.4$ layer ($x_{La} = 0.6166$) consistent with the restraint of a total 1.5 La and 1.5 Ca atoms per unit cell. From the compound stoichiometry, the intermixing of Ca on the A'' site demands that some Y must relocate to the A' site. Given a 50% mixture of Ca and Y on the A'' site, each A' site should have 0.25 Y, 0.25 Ca, and 0.5 La. This does suggest more intermixing on the A cation sites than is represented by a strict large/small A'/A'' ordering. The result that the occupation at the A'' site is by a lighter element (smaller Z) than at A' is nevertheless overall consistent with a preference for occupying the A' site with La, and the A'' with Y.

Concerning the B-cation ordering, the refinement in Table 3 for the undoped compound shows a best fit for Cu occupancies near the correct value of zero. By comparison, the refined Cu occupancy is 0.24 on the $z = 0.3$ layer for the doped compound for a refined doping level of $x = 0.48$ (Table 4). The $z = 0.5$ Cu occupancy is refined to $x_{Cu} = 0.0$. Figures 12a and 12b show the variances of R with respect to the $z = 0.3$ Cu occupancy in the undoped and doped cases. In the undoped case, the refined minimum of 0.08 for the occupancy parameter is evidently not statistically differentiable from zero, because it is known that the correct value in this case is zero. While Fig. 12 gives a sense of the breadth of

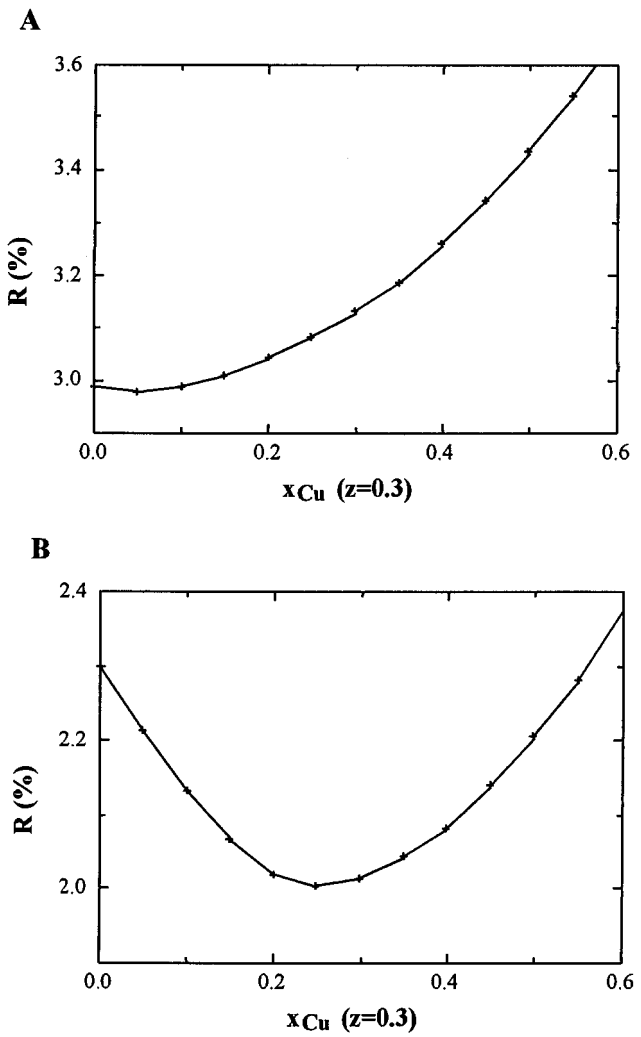

FIG. 12. *R* factor vs copper occupancy in the $z = 0.3$ layer for the undoped (top figure) and $x = 0.6$ doped (bottom figure) members of the $LaYCaBa_2Cu_{2+x}Ti_{3-x}O_{14-y}$ system. Note that the minimum in *R* factor occurs near zero for the undoped material, as expected, and near 0.3 in the doped material, which is consistent with preferential copper segregation to the top and bottom layers.

the *R* value minima for this technique, reliable error values can only be obtained via an assessment of the errors on measured intensity data. As this would require measurement of multiple through-focus series, it was not performed. While the present refinements do suggest that Cu may preferentially locate on the $z = 0.3$ compared with the $z = 0.5$ layer, it should be noted that the present refinement results are dependent on the assumption that all oxygen vacancies are located on the Ba layer. In refinements in which the oxygen positions were left fully occupied, or in which the oxygen vacancies were statistically distributed on all oxygen sites, the resulting Cu occupancies differed significantly from those shown in Tables 3 and 4. Nevertheless, the strong argument for a nonrandom oxygen vacancy distribution (the constraint that the Ti coordination with oxygen be intact) supports the model's assumption. In light of this, the HRTEM results provide support for the random top/bottom layer model for the Cu and oxygen vacancy distribution. Figures 13a to 13f show a comparison of the symmetrized experimental projections with the best-match solutions from the genetic algorithm for the $x = 0.6$ specimen through-focus series. The traces shown are those for the refinement summarized in Table 4. The fits in the case of the undoped compound were similar, although not quite as good, as reflected in the slightly higher *R* factor.

CONCLUSIONS

The compounds $Eu_2CaBa_2Cu_2Ti_3O_{14}$ and $LaYCaBa_2Cu_{2+x}Ti_{3-x}O_{14-y}$ are non-superconducting layered cuprates, in spite of a layered structure with copper oxygen bond lengths similar to the known superconductors. No evidence for superconductivity exists in the conductivity, thermopower, or magnetic property data. Undoped $Eu_2CaBa_2Cu_2Ti_3O_{14}$ and $LaYCaBa_2Cu_2Ti_3O_{14}$ are lightly-doped *p*-type semiconductors at high temperatures. The exact origin of these carriers is undetermined, though it is likely due to fluctuations in the cation stoichiometry. The large–small rare-earth perovskite ($LaYCaBa_2Cu_2Ti_3O_{14}$) exhibits more extrinsic electrical property behavior than the large–large rare-earth perovskite ($Eu_2CaBa_2Cu_2Ti_3O_{14}$). All of these observations are consistent with the behavior observed in the quadruple perovskites.

Oxygen interstitials can intercalate between the adjacent copper–oxygen sheets in large–large rare-earth perovskites, whereas oxygen intercalation in large–small rare-earth perovskites is energetically unfavorable. This appears in the oxygen partial pressure dependence of the electrical property data and is similar to the observations in the quadruple perovskites. Substitution with (Cu''_{Ti}) results in ionic compensation in $LaYCaBa_2Cu_{2+x}Ti_{3-x}O_{14-y}$ throughout the entire doping range $0.0 \leq x \leq 0.4$. Rather than the desired electronic compensation mechanism with hole carriers, oxygen vacancies ($V^{\bullet\bullet}_o$) are introduced in a 1:1 ratio with copper substituents. These oxygen vacancies cannot be refilled with subsequent intermediate temperature oxygen anneals.

In accordance with the preferred coordination environments of copper and titanium, probable vacancy arrangements have been proposed. A vacancy model in which the copper dopants segregate to the first and third layer of the quintuple perovskite seems the most likely and is consistent with the electrical property and HRTEM data.

APPENDIX

The derivation of text Eqs. [4] and [7] employs text Eqs. [1], [3], [5], and [6]. The electroneutrality condition of

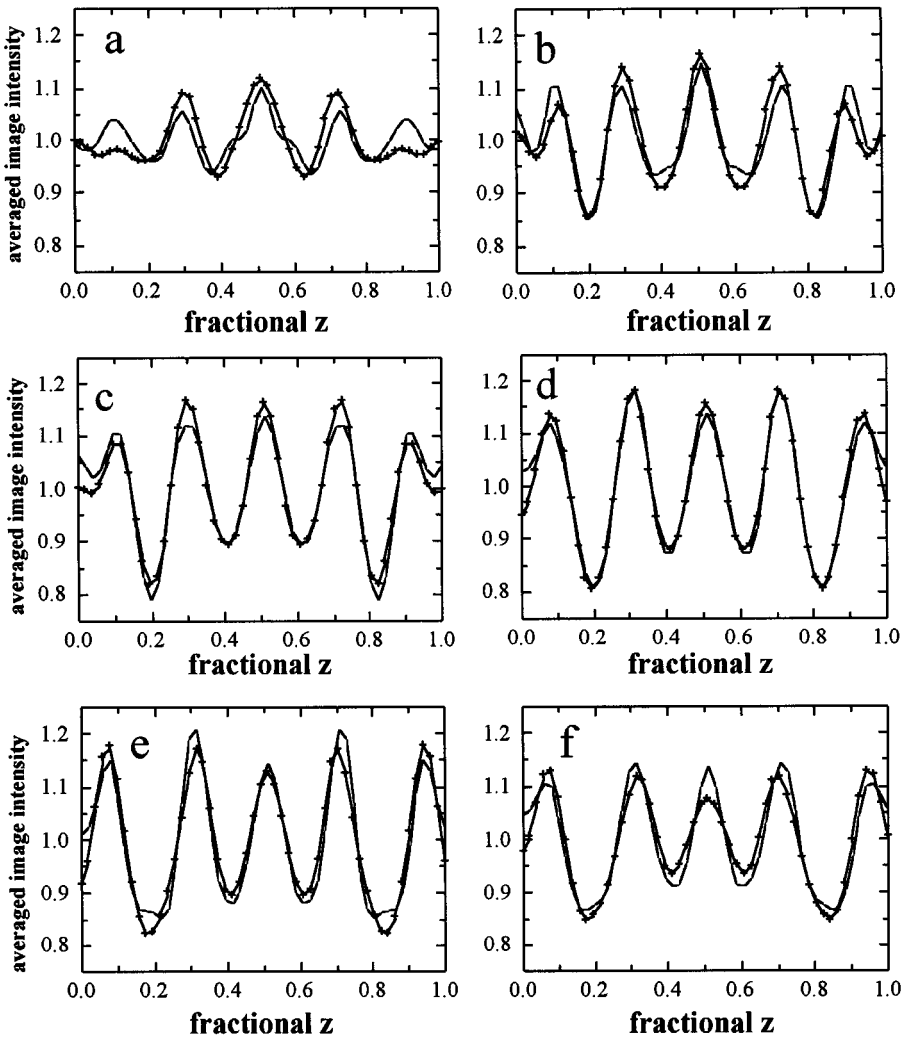

FIG. 13. Calculated (−) vs experimental (- + -) projected HRTEM intensities for the $x = 0.6$ doped specimen. The calculated curves correspond to the parameters in Table 4. The defoci are given by defocus start for (a) − 286 Å and a defocus step between images of − 109 Å (underfocus negative).

Eq. [6] (unintentional donors and acceptors are ignored) can be written as

$$[O_i''] = \tfrac{1}{2}(p - n). \qquad [A1]$$

Inserting this into Eq. [1] we obtain:

$$K_O P_{O_2}^{1/2} = \tfrac{1}{2}(p - n)p^2. \qquad [A2]$$

By introducing the variable, a, from Eq. [3] we can express p and n in terms of a, i.e., $p = an_i$, where n_i is the intrinsic carrier concentration and $n = a^{-1}n_i$. The two-band conductivity of a sample is related to the carrier concentrations by

$$\sigma = ne\mu_e + pe\mu_h. \qquad [A3]$$

Assuming the mobilities to be the same for electrons and holes, based on the approximate symmetry of Jonker pears for most layered cuprates (11),

$$\sigma = e\mu(n + p). \qquad [A4]$$

Substituting the expressions involving a into Eq. [A4] we obtain

$$\sigma = e\mu\left(an_i + \frac{1}{a}n_i\right) = e\mu n_i\left(a + \frac{1}{a}\right). \qquad [A5]$$

However, it can be shown that $\sigma_i = 2n_i e\mu$. Hence,

$$\sigma = \tfrac{1}{2}\sigma_i\left(a + \frac{1}{a}\right). \qquad [A6]$$

Substituting the various expressions for involving a into Eq. [A2] we arrive at

$$K_O P_{O_2}^{1/2} = \tfrac{1}{2}\left(an_i + \frac{1}{a}n_i\right)a^2 n_i^2 = \tfrac{1}{2}n_i^3 a(a^2+1). \quad [A7]$$

We now have expressions for the conductivity and the intrinsic carrier concentration in terms of material parameters and a single constant, a. We can solve for a in terms of conductivity and plug this into the pO_2 expression, but the math becomes cumbersome. Instead, the chain rule can be employed:

$$\frac{d\ln\sigma}{d\ln P_{O_2}} = \frac{d\ln\sigma}{da}\frac{da}{d\ln P_{O_2}}. \quad [A8]$$

Taking the derivative of both sides of Eq. [A6] with respect to a yields

$$\frac{d\ln\sigma}{da} = \frac{a^2-1}{a(a^2+1)}. \quad [A9]$$

Similarly, the derivative of Eq. [A7] with respect to a gives

$$\frac{d\log P_{O_2}}{da} = \frac{2(3a^2+1)}{a(a^2+1)}. \quad [A10]$$

Substitution of Eqs. [A9] and [A10] into Eq. [A8] yields

$$\frac{d\ln\sigma}{d\ln P_{O_2}} = \frac{(a^2-1)^2}{2(a^2+1)(3a^2+1)}, \quad [A11]$$

which is Eq. [4]. Solving Eq. [A6] in terms of a yields

$$a = \frac{\sigma}{\sigma_i} + \sqrt{\frac{\sigma^2}{\sigma_i^2} - 1}, \quad [A12]$$

which is the same as Eq. [7].

ACKNOWLEDGMENTS

This work was supported by the National Science Foundation (DMR 91-20000) through the Science and Technology Center for Superconductivity and made use of MRL Central Facilities supported by the National Science Foundation, at the Materials Research Center of Northwestern University (Award No. DMR-9120521) One of the authors (K.O.) is partly supported by a research fellowship of the Japan Society for the Promotion of the Science for Young Scientists.

REFERENCES

1. J. G. Bednorz and K. A. Müller, *Z. Phys. B.* **64,** 189 (1986).
2. P. A. Salvador, T. O. Mason, K. Otzschi, K. B. Greenwood, K. R. Poeppelmeier, and B. Dabrowski, *J. Am. Chem. Soc.* **119,** 3756 (1997).
3. M. R. Palacin, F. Krumeich, M. T. Caldes, and P. Gomez-Romero, *J. Solid State Chem.* **117,** 213 (1995).
4. M. R. Palacin, A. Fuentes, N. Casan-Pastor, and P. Gomez-Romero, *Adv. Mater.* **6,** 54 (1994).
5. P. Gomez-Romero, M. R. Palacin, and J. Rodriguez-Carvajal, *Chem. Mater.* **6,** 2118 (1994).
6. P. A. Salvador, L. Shen, T. O. Mason, K. B. Greenwood, and K. R. Poeppelmeier, *J. Solid. State Chem.* **119,** 80 (1995).
7. J. B. Goodenough, *Supercond. Sci. Technol.* **3,** 26 (1990).
8. A. Gormezano and M. T. Weller, *Physica C* **235–240,** 999 (1994).
9. M. R. Palacin, N. Casau-Pastor, G. Kramer, M. Jansen, and P. Gomez-Romero, *Physica C* **261,** 71 (1996).
10. P. A. Salvador, Ph.D. dissertation, Northwestern University, 1997.
11. P. Gomez-Romero, M. R. Palacin, C. R. Michel, and N. Casan-Pastor, *Solid State Ionics* **101,** 411 (1997).
12. W. J. Zhu, Y. Z. Huang, T. S. Ning, and Z. X. Zhao, *Mater Res. Bull.* **30,** 243 (1995).
13. K. D. Otzschi, K. R. Poeppelmeier, P. A. Salvador, T. O. Mason, H. Zhang, and L. D. Marks, *J. Am. Chem. Soc.* **118,** 8951 (1996).
14. P. A. Salvador, K. Otzschi K., H. Zhang, J. R. Mawdsley, K. B. Greenwood, B. M. Dabrowski, L. D. Marks, T. O. Mason, and K. R. Poeppelmeier, *Mater. Res. Soc. Symp. Proc.* **453,** 311 (1997).
15. M. J. Pack, A. Gormezano, and M. T. Weller, *Chem. Mater.* **9,** 1547 (1997).
16. M.-Y. Su, C. E. Elsbernd, and T. O. Mason, *J. Am. Ceram. Soc.* **73,** 415 (1990).
17. L. Shen, P. A. Salvador, and T. O. Mason, *J. Phys. Chem. Solids* **57,** 1311 (1996).
18. G. W. Tomlins, N.-L. Jeon, T. O. Mason, D. A. Groenke, J. T. Vaughey, and K. R. Poeppelmeier, *J. Solid State Chem.* **109,** 338 (1994).
19. G. H. Jonker, *Philips Res. Repts.* **23,** 131 (1968).
20. G. Brouwer, *Philips Res. Repts.* **9,** 366 (1954).
21. A. Trestman-Matts, S. E. Dorris, and T. O. Mason, *J. Am. Ceram. Soc.* **66,** 589 (1983).
22. D. S. McLachlan, M. Blaskiewicz, and R. E. Newnham, *J. Am. Ceram. Soc.* **73,** 2187 (1990).
23. M. H. Kane, M.S. dissertation, Northwestern University, 1997.
24. K. B. Greenwood, G. M. Sarjeant, K. R. Poeppelmeier, P. A. Salvador, T. O. Mason, B. Dabrowski, K. Rogacki, and Z. Chen, *Chem. Mater.* **7,** 1355 (1995).
25. P. A. Salvador, K. B. Greenwood, K. Otzschi, J. W. Koenitzer, B. M. Dabrowski, K. R. Poeppelmeier, and T. O. Mason, *Mater. Res. Soc. Symp. Proc.*, **453,** 171 (1997).
26. K. D. Otzschi, D. Vander Griend, K. R. Poeppelmeier, W. Sinkler, L. D. Marks, and T. O. Mason, *Chem. Mater.* **10,** 2579 (1998).
27. R. D. Shannon, *Acta Crystallogr., Sect. A* **32,** 751 (1976).
28. M. J. Pack and M. T. Weller, *Physica C* **282–287,** 751 (1997).
29. W. E. King and G. H. Campbell, *Ultramicroscopy* **56,** 46 (1994).
30. H. Zhang, L. D. Marks, Y. Y. Wang, H. Zhang, V. P. Dravid, P. Han, and D. A. Payne, *Ultramicroscopy* **57,** 103 (1995).
31. G. Möbus, *Ultramicroscopy* **65,** 205 (1996).
32. G. Möbus and G. Dehm, *Ultramicroscopy* **65,** 217 (1996).
33. S. Kirkpatrick, C. D. Gelatt, and M. P. Vecci, *Science* **220,** 671 (1984).
34. J. H. Holland, "Adaptation in Natural and Artificial Systems." University of Michigan Press, Ann Arbor, MI, 1975.